

PAPER • OPEN ACCESS

A penetration efficiency model for the optimization of solid conical microneedles' geometry

To cite this article: Leonardo Piccolo *et al* 2024 *J. Micromech. Microeng.* **34** 025009

View the [article online](#) for updates and enhancements.

You may also like

- [Polymer microneedles integrated with glucose-responsive mesoporous bioactive glass nanoparticles for transdermal delivery of insulin](#)
Guohua Jiang, Bin Xu, Jiangying Zhu et al.
- [Development of SU-8 hollow microneedles on a silicon substrate with microfluidic interconnects for transdermal drug delivery](#)
Richa Mishra, Tapas Kumar Maiti and Tarun Kanti Bhattacharyya
- [Development of a drug-coated microneedle array and its application for transdermal delivery of interferon alpha](#)
Kosuke Kusamori, Hidemasa Katsumi, Ryota Sakai et al.



ECS
The
Electrochemical
Society
Advancing solid state &
electrochemical science & technology

DISCOVER
how sustainability
intersects with
electrochemistry & solid
state science research

A penetration efficiency model for the optimization of solid conical microneedles' geometry

Leonardo Piccolo, Kristal Bornillo*, Sara Micheli, Marco Sorgato, Mauro Ricotta, Elisa Cimetta and Giovanni Lucchetta

Department of Industrial Engineering, University of Padua, 35131 Padova, Italy

E-mail: kristalubrey.bornillo@studenti.unipd.it

Received 5 October 2023, revised 26 December 2023

Accepted for publication 12 January 2024

Published 23 January 2024



Abstract

Microneedles (MNs) are promising alternatives to pills and traditional needles as drug delivery systems due to their fast, localized, and relatively less painful administration. Filling a knowledge gap, this study investigated and optimized the most influential geometrical factors determining the penetration efficiency of MNs. The effects of height, base diameter, and tip diameter were analyzed using the finite element method, with results showing that the most influencing factor was base diameter, followed by height. Moreover, the taper angle, which is dependent on all the geometrical factors, was found to directly affect the penetration efficiency at a fixed height. An additional model was developed to relate the height and taper angle to penetration efficiency, and the results were experimentally validated by compression testing of MN array prototypes printed using two-photon photolithography. The numerical model closely predicted the experimental results, with a root mean square error of 9.35. The results of our study have the potential to aid the design of high-penetration efficiency MNs for better functionality and applicability.

Supplementary material for this article is available [online](#)

Keywords: optimizations, conical, microneedles, penetration efficiency, numerical modeling, transdermal drug delivery

1. Introduction

The use of drug delivery systems (DDS), along with sampling and diagnostics, is crucial to therapeutic procedures. Drug delivery routes can be in the form of oral administration, which, despite being the most popular, is prone to drug degradation, poor absorption through the intestinal walls, or

long-term kidney and liver side effects [1]. Another common DDS is the intravenous, intramuscular, or subcutaneous injection with the use of needles; despite being a rapid and efficient method, it causes pain to the patients and cannot sustain long-term and continuous delivery [1, 2]. Another alternative is transdermal delivery, based on the direct application of drugs on the skin; drugs should penetrate through the stratum corneum (SC), the viable epidermis, and finally into the dermis, where they are available for absorption [3]. Most medications cannot enter the body through the skin at therapeutic rates due to the 10–20 μm thick SC that acts as a barrier and the presence of keratinized dead cells and scales, all severely constraining the use of this method [4]. The skin's permeability is dramatically increased if the SC layer

* Author to whom any correspondence should be addressed.



Original content from this work may be used under the terms of the [Creative Commons Attribution 4.0 licence](#). Any further distribution of this work must maintain attribution to the author(s) and the title of the work, journal citation and DOI.

is punctured. Several methods have been investigated to disrupt the layer, including the use of chemical or lipid enhancers [5, 6], electric fields using iontophoresis and electroporation [7], pressure waves produced by ultrasound, and photoacoustic effects [8]. However, because chemical methods can have adverse effects both on the skin and the drugs, and because physical methods require sophisticated systems, they only had a limited influence on medical practices to date.

Microneedles (MNs) are an effective method for transdermal delivery because they can penetrate the SC without harming the skin or the drug and without needing an energy source or other complex systems. MN also offers the advantages of easy self-administration, localized action, and few adverse systemic effects. These make them a promising alternative to pills, traditional needles, or other transdermal patches for minimally invasive drug delivery [9–11].

MN are often fabricated using materials such as silicon, stainless steel, or polymers and can be classified as solid, hollow, coated, or dissolvable [2]. A single MN elicits less pain than hypodermic needles, also when used in an arrayed configuration in a patch [12–14]. Haq *et al* [14] evaluated 12 human subjects' pain and sensory response following the single-blinded insertions of a 25-G hypodermic needle and two silicon MN arrays (of 180 and 280 μm height). The subjects reported significantly less pain and discomfort with MN arrays, confirming that MN can penetrate the SC without reaching the pain receptors deep in the dermis, unlike hypodermic needles.

The geometry of MNs must be carefully considered to make sure that they can successfully penetrate the skin to deliver their drug load efficiently and without causing pain. Height, base diameter, tip radius, tip angle, and needle shape, define the geometry of a MN. Several experimental studies have shown the effects of MN geometry on skin penetration [15–21], revealing trends helping to understand the key elements influencing MN insertion. For example, one study found that a cone is the optimal shape of MNs for ovalbumin delivery in terms of skin insertion ratio [20], and the same shape was observed to have the optimal penetration depth in human skin [16]. Moreover, conical MNs were also observed to have better mechanical stability and penetration capabilities as compared to pyramidal MNs [22]. Uppuluri *et al* [23] studied the effect of MN height (600, 900, 1200, and 1500 μm) on the transdermal delivery of Zolmitriptan, and showed that increasing the needle height increased the drug permeation into pig ear skin. This is to be expected because longer needles deliver drugs more deeply, and deeper drug delivery increases the likelihood that the drug will reach the dermal layer and be available for absorption by the microcirculation. However, there is a limit to the height of MN since a three-fold increase in height results in a seven-fold increase in pain [12].

For effective drug delivery, the height of the MNs should be optimized to allow drug release in the viable epidermis or very top of the dermis, where drug binding, metabolism, and active transport occur, while not reaching the pain receptors deep in the dermis. The increase in height does not necessarily improve the MN penetration efficiency, defined here

as the ratio of the inserted length over the designed length as in equation (1), which also depends on other parameters [23, 24]. Donnelly *et al* [25] applied poly(methyl vinyl ether-co-maleic anhydride, PMVE/MA) MN arrays of heights 280, 350, 600, and 900 μm into neonatal porcine skin *in vitro* and measured penetration efficiencies of 91.6%, 83.71%, 78.36%, and 87.62%, respectively. The authors proved that penetration depth does not directly correlate with penetration efficiency, as full penetration is uncertain due to factors such as skin elasticity and irregularity and MN geometrical settings [1]

$$\text{Penetration efficiency} = \left(\frac{\text{inserted length of MN}}{\text{designed length of MN}} \right) \times 100\%. \quad (1)$$

All the cited studies focused on optimizing MN geometrical factors for drug release, penetration depth, and insertion force. However, it is rare to see MN geometry optimization with respect to penetration efficiency. Moreover, previous research focused only on a single or a combination of two geometrical factors to design and optimize MN. There is still no existing study on the combined optimization of base diameter, tip diameter, and height on the penetration efficiency of an MN.

In this study, the most influential geometrical parameters of solid conical MNs for effective penetration into an artificial skin were investigated and optimized using the finite element method implemented in Ansys. A model was developed to describe the relationships between the geometrical factors and the penetration efficiency. The numerical analysis results were validated against experimental data obtained with MN patch prototypes fabricated using two-photon lithography and tested on polydimethylsiloxane (PDMS) artificial mimics of human skin. The numerical analysis narrowed down the significant geometrical factors from three to two, generating a model with taper angle and height as factors that can be manipulated to optimize penetration efficiency. Specifically, constraining the height to a constant level, the penetration efficiency is inversely correlated with the taper angle, and this was validated through experimental results. The results of this study can be used in designing and predicting the performance of MN arrays in terms of penetration efficiency to tailor them to the specific intended application.

2. Methods

2.1. Numerical modeling of the MN penetration

Figure 1 illustrates the layers of human skin, i.e. the epidermis, the outermost layer that plays a barrier role; the dermis, where nerve cell terminals are located; and the subcutaneous fat layer, the primary fat reservoir.

The SC is the 12–20 μm thick upper layer of the epidermis. It is composed of dead epidermal keratinocytes, flattened cells, and intracellular lipid lamellae that form a biological barrier preventing excessive water loss and defending the organism from external agents of both physical and bacterial nature [26].

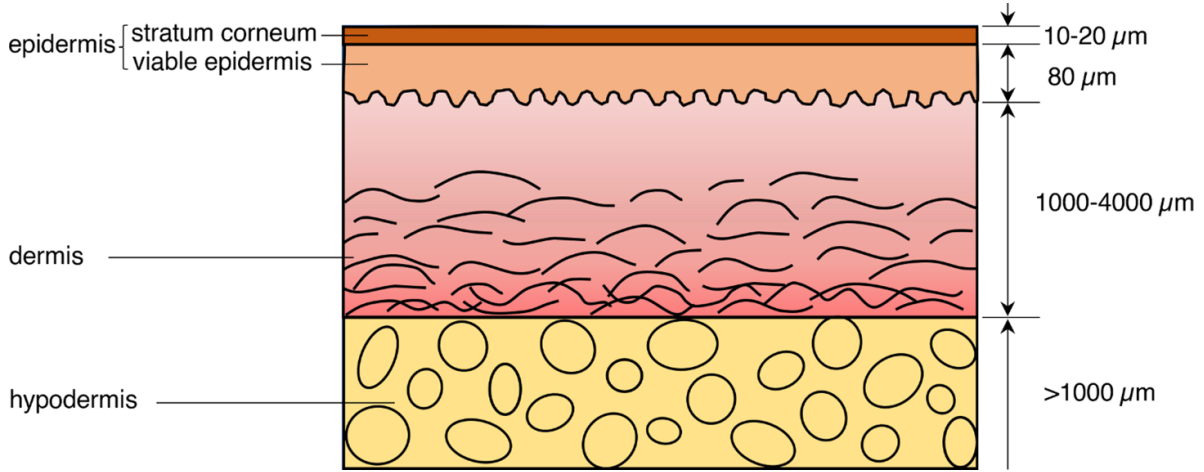


Figure 1. Schematic diagram of human skin tissue model showing the thickness of the layers.

Of interest to our study, it also hinders the passage of substances containing the drug to be administered. The dermis is composed of collagen fibers that become less and less dense with depth and is responsible for the thermal and mechanical properties of the skin; the dermis is also the location of the first transducers of pain. The hypodermis largely comprises adipocytes that serve as thermal insulation for the body and energy reserve [27]. For effective drug delivery, the MN must penetrate the epidermis and the dermis without reaching the hypodermis, not to stimulate pain receptors. This depth is located about 1 mm from the surface.

Silicone rubber was selected for the numerical simulations and the experimental tests to mimic human skin behavior. Among the various types of elastomers used for this type of testing, silicone rubber comes closest to the characteristics of human skin in terms of tear and tensile strength. Also, it does not exhibit crystallization upon deformation [28, 29].

We used PDMS produced by Dow Corning (Sylgard 184) at a 5:1 ratio of pre-polymer and curing agent based on the determination of its bulk mechanical properties by uniaxial tensile tests. For this study, a material model that minimizes the number of parameters while accurately representing the experimental data was used. A tool included in the Ansys simulation suite version 18.2 was used to test the accuracy of different material models. Specifically, the Yeoh third-order representation was chosen to model the results of the tensile tests after an initial visual examination of how several material models reflected the experimental data [30].

The Yeoh material is described by equation (2):

$$W = \sum_{i=1}^N C_{i0} (\bar{I}_1 - 3)^i + \sum_{i=1}^N \frac{1}{D_i} (J - 1)^{2i} \quad (2)$$

where J is the volume ratio before and after deformation, W is the strain energy density function, and \bar{I}_1 is the first invariant of the Cauchy–Green strain tensor. $N = 3$ for a third-order Yeoh material. Shear isochoric strain energy density is the term on the left, while volumetric strain energy density is on the right.

As the hyperelastic material was considered incompressible, we set $J = 1$. Specific material parameters are C_{10} , C_{20} , C_{30} , D_1 , D_2 , and D_3 , where C_{10} makes up half of the initial bulk modulus, and $1/D_i$ makes up half of the initial shear modulus, with values tabulated in supplementary table S1.

In this model, a solid conical MN was used as the base design, as shown in figure 2(a). An acrylic polymer (IP-S, Nanoscribe) was chosen as the fabrication material for numerical and experimental studies. The material properties used to model its elastic behavior were Young's modulus of 2.1 GPa, Poisson's ratio of 0.3, and tensile strength of 64.5 MPa [31].

To identify the most influential geometrical factors of MN penetration, the height (H), base diameter (D_b), and tip diameter (D_t) were varied in settings according to the Design of the Experiment (DoE) reported in the table in figure 2(b). This sums up to a total of 12 simulations.

The finite element simulation of the insertion process of the MN into the skin was carried out using the finite element code Ansys Workbench in the Explicit Dynamics function combined with the element deletion algorithm. In the element deletion method, an element volume is deleted when it meets the required condition during deformation, in this case, the von Mises stress failure criterion. The von Mises stress failure criterion was derived by relating the distortion energy in a unit volume during needle insertion simulation with the distortion energy per unit volume calculated from the prior tensile results done with the PDMS sample. This setting was chosen because it deals with events that occur in a short time on hyperelastic materials with non-linearity due to large deformations and breakage of the material. In this study, the location of the deleted elements was mainly at the area being penetrated by the needle, an example of an image of the needle penetration with deleted elements from the skin is shown in supplementary figure S1(a).

Given the axisymmetric geometry of the single MN, the numerical model used to analyze penetration was set up by exploiting a simplified 2D geometry. The simplification considerably reduced the computational time. The geometry and

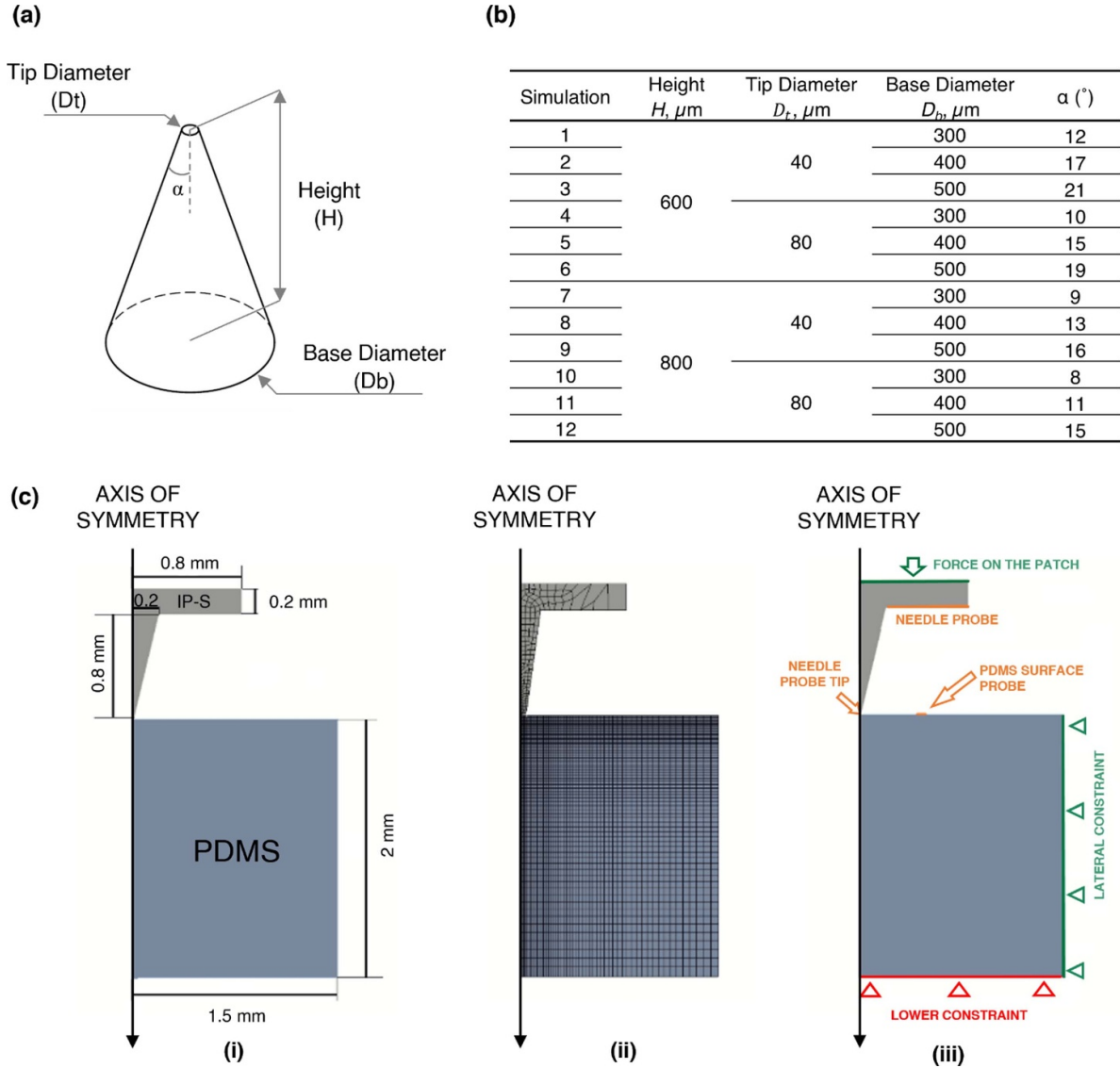


Figure 2. (a) Geometric settings of the numerical simulations; (b) the geometry of a single conical microneedle; (c) simulation setup showing (i) the size of the material domains, (ii) the 2D meshes for the needle and PDMS artificial skin, and (iii) the load distribution and constraints on both lateral and bottom boundaries. The tip radius is $20 \mu\text{m}$. Measurements shown are in millimeters.

boundary conditions employed in the numerical simulation are shown in figure 2(c). The PDMS material was constrained in both the lateral and bottom skin boundaries. The tapered MN was constrained to move along the insertion direction (normal to the skin surface) under a constant force of 0.247 N according to the assumption of considering a patch of 81 needles and applying a 20 N force on the whole patch. The coefficient of friction between the IP-S MN and PDMS skin mimic was set at 0.48 .

Before the numerical simulations, the optimal size of the needle and skin mesh were determined by varying them according to supplementary table S2. For all settings, an axisymmetric mesh consisting of quadrilateral elements, with a curvature size function, was used for each setting to obtain a more accurate numerical solution in the high-stress and strain gradient zone. In the first setting L1, the needle and artificial skin elements were set to a minimum size of $3 \times 10^{-2} \text{ mm}$.

For L2, the needle element size was reduced to $2 \times 10^{-2} \text{ mm}$, while keeping the skin element size the same as in L1. Finally in L3, both the needle and skin element size were reduced to $1 \times 10^{-2} \text{ mm}$. Figure S1 shows the results of the mesh sensitivity analysis. A negligible difference in displacement was observed between all settings, as shown in figure S1(b). However, figure S1(c) shows a higher skin strain in L1 and a small difference between L2 and L3. Between L2 and L3, however, L3 shows a more precise stress trend, as observed with lower stress peaks in figure S1(d). Mesh setting L3 was chosen as the final mesh for all succeeding numerical simulations.

2.2. Experimental validation

2.2.1. MNs design and fabrication. Based on the results obtained from the numerical analysis, physical prototypes of the MNs were fabricated and tested for their penetration into

Table 1. MN array prototypes dimensions.

Sample	D_b , (μm)	α , ($^\circ$)	H , (μm)
1	300	11	771
2	400	15	746
3	400	20	549
4	400	25	429

artificial skin as 4×4 MN arrays. The pitch was selected based on the previous study by Shu *et al* [32], wherein it was shown that the penetration efficiency and force increase and decrease, respectively, with increasing pitch from 0.156 mm to 0.5 mm. Beyond 0.5 mm until 1.75 mm, no significant change in both penetration efficiency and force was observed, which means that the pitch no longer affects the efficiency and force. For this study, a pitch of 1 mm was chosen to allow enough needle-to-needle distance while also knowing that the efficiency is at optimum. Four patches with different tip angle values ($\alpha = 11^\circ$, 15° , 20° , and 25°) were designed according to table 1. Also shown are their base diameters and corresponding height. Sample 1 has a different base diameter to not surpass the $800 \mu\text{m}$ set limit of painless penetration (the $400 \mu\text{m}$ value with taper angle $= 11^\circ$ would result in a $1.029 \mu\text{m}$ height).

The samples were first designed as 3D models according to the dimensions in table 1. The MNs were precisely fabricated from the CAD models using an ultrafine maskless two-photon polymerization (2PP) 3D laser lithography machine (Photonic Professional GT, Nanoscribe GmbH, Germany). The laser light source has a wavelength of 780 nm , a pulse width of 150 fs , a frequency of 40 MHz to 100 MHz , and a maximum of 45 mW . The objective used has a $25\times$ magnification.

The MN arrays were printed from IP-S photoresist directly on a glass substrate. The IP-S is a negative-tone and acrylate-based photoresist from Nanoscribe GmbH and has Young's modulus of 2.1 GPa [31]. The IP-S resin was placed on ITO-coated glass slides and inserted into the platform with the lens immersed in the resin. After printing, the unpolymerized excess resin was removed by soaking the sample in the developer propylene glycol methyl ether acetate for 30 min . The sample was then transferred to another beaker containing isopropanol and soaked for 3 min to remove all developer residues from the sample. Finally, it was allowed to dry in ambient conditions before testing.

2.2.2. Penetration tests. Analogously to the numerical analyses, the PDMS Sylgard 184 with a 5:1 ratio of pre-polymer and curing agent was used as artificial skin in the experimental campaign. Briefly, the two components were weighted and mixed until a homogeneous mixture was obtained; all formed air bubbles must be removed using a desiccator prior to casting in the desired shape and finally curing in a convection oven at 75°C for at least 120 min .

Insertion force and displacement of the IP-S needles into the PDMS artificial skin were measured using a tribometer (UMT-3, CETR Ltd, USA). Its piezoelectric actuator in the vertical axis provided a displacement control resolution of

$2 \mu\text{m}$, and the load cell allowed a resolution of 5 mN , with a full scale of 100 N .

The glass slide with the printed MNs was placed on the top portion of the tribometer 3 mm from the surface of the PDMS samples. The penetration test was done at a set displacement of 3 mm and a speed of 0.5 mm s^{-1} . An additional distance of 0.5 mm was added to account for the compression of the soft PDMS and to make sure that the needles penetrated it. For every new test, the same displacement of the glass slide was set, and the load cell was zeroed before the test. All penetration tests were done with three replicates for each type of tip angle.

After the penetration test, images of the MNs were obtained using a scanning electron microscope (SEM) to verify if they suffered any deformation. Finally, both the simulation and experimental results were analyzed and compared.

2.3. Results and discussion

2.3.1. Numerical simulation. The simulated insertions of the MN with varying geometrical parameters into the artificial skin are shown as vertical displacement versus time in figure 3(a). The profiles are characterized by two zones with different slopes: the first describes the MN penetration into the PDMS artificial skin, characterized by an increasing insertion depth with time, and the second, in which the insertion depth can be considered constant indicates that the needle is not penetrating any farther into the PDMS, identified as the end of penetration. In agreement with previous publications, increasing the MN height increases penetration depth [25, 33]. Interestingly, despite the differences in geometrical configurations, the final insertion depths of all samples ranged from 440 to $760 \mu\text{m}$ and correctly punctured the SC. Moreover, it was observed that a combination of the smallest base diameter ($300 \mu\text{m}$) and longest needle length ($800 \mu\text{m}$) had the deepest penetration regardless of the tip diameter. On the other hand, the shallowest penetration depth is a combination of the largest base diameter ($600 \mu\text{m}$) and shortest needle length ($600 \mu\text{m}$), also regardless of tip diameter. Overall, our modeling results suggest that the base diameter's influence on MN's penetration depth is stronger than that of the tip diameter, and that smaller base widths correlate with deeper penetration.

To further prove our observations and determine each factor's relative strength on the MN's penetration efficiency, we used the main effects plot shown in figure 3(b). The strong correlation between the base diameter (D_b) and the penetration efficiency is clear, where smaller base values determine a higher penetration of the MN, according to the fact that increasing widths would require larger insertion forces [34]. Although not to the same degree as the base diameter, the height also influences penetration efficiency. Particularly, having a shorter height has higher efficiency than having a longer one. The same trend was observed by Donnelly *et al* [25] when they increased the height from $350 \mu\text{m}$ to $600 \mu\text{m}$. However, the trend changed and the penetration efficiency increased when the height was further increased to $900 \mu\text{m}$. In another study by Lim *et al* [35], penetration efficiency increases with height change from $400 \mu\text{m}$ to $800 \mu\text{m}$, then a significant

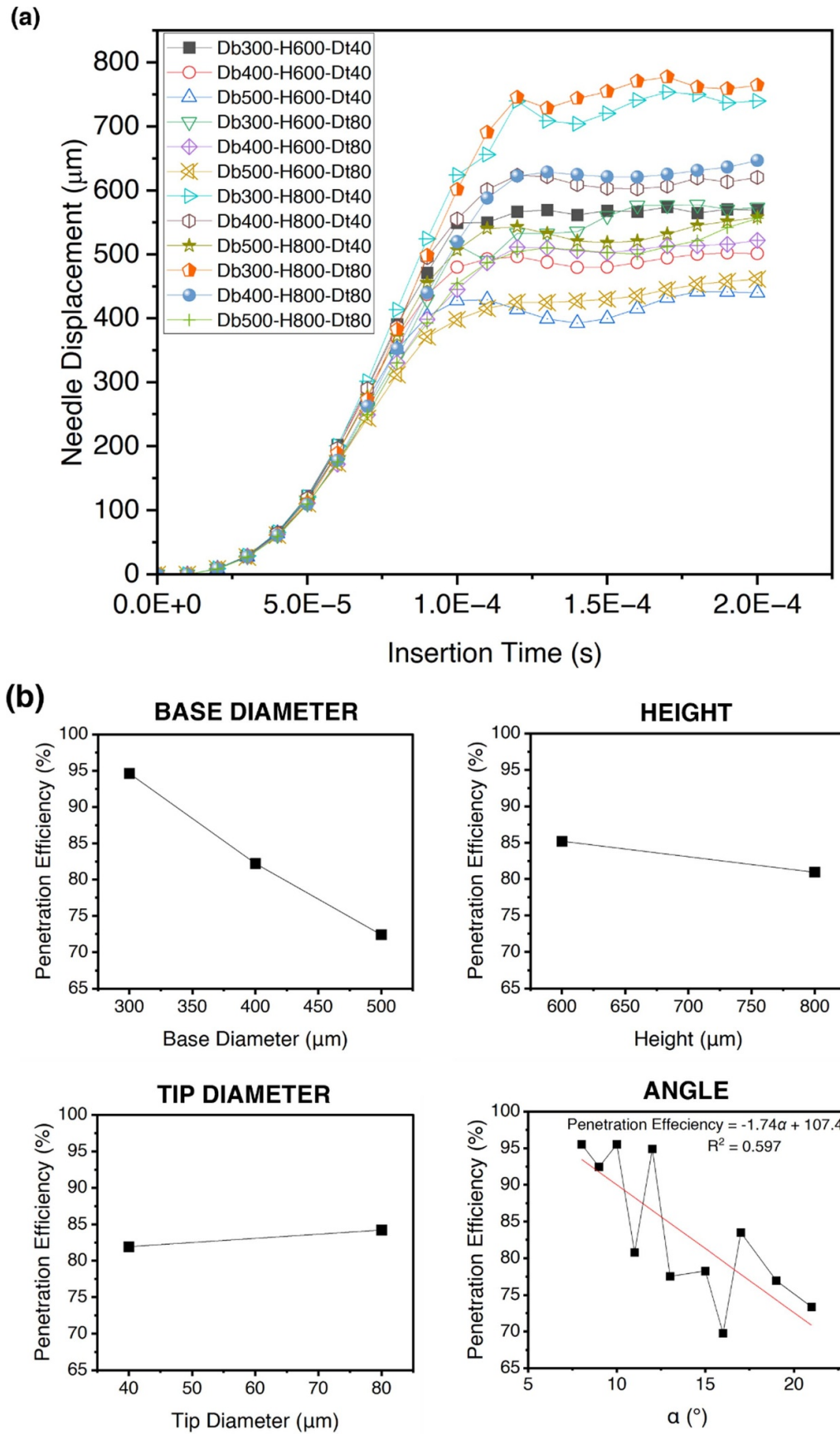


Figure 3. (a) Insertion depths of the microneedle for the 12 different simulations. (b) Effect of geometrical factors on penetration efficiency.

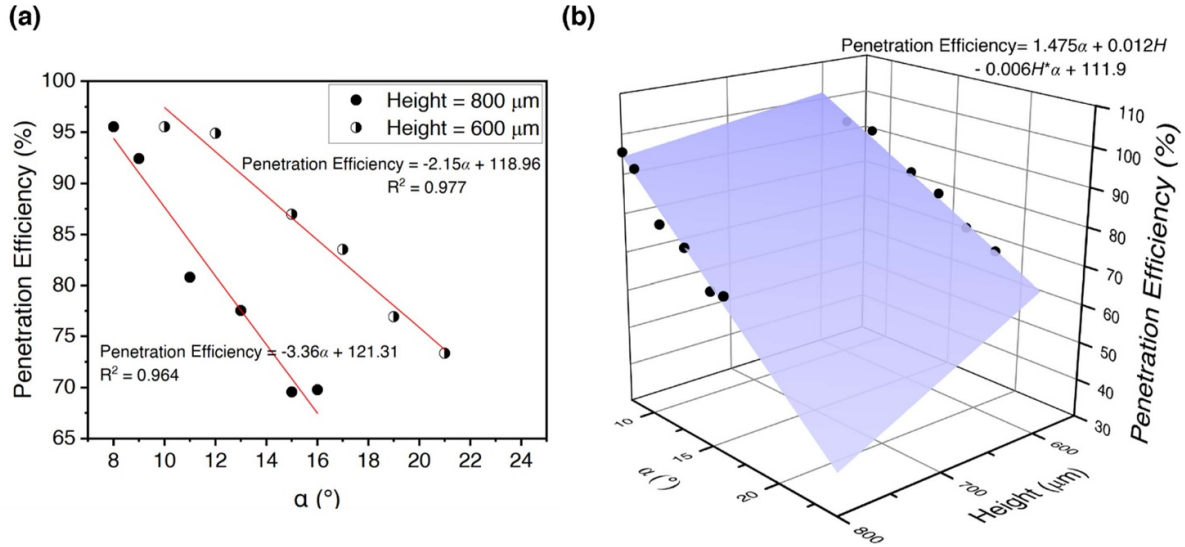


Figure 4. (a) Linear regression between the taper angle and penetration efficiency grouped by height, and (b) the generated surface plot and model of the two linear equations based on simulation (black circular dots).

decrease in efficiency was observed at MN height of 1200 μm . The differences in the effect of height on the penetration may be due to the friction, buckling, and breakages that occur during penetration which may cause differences in results, especially when comparing different materials. The change in tip diameter does not show as much difference as changing the base diameter or the height. This is in agreement with a study by Lim *et al* [35], wherein they also observed an insignificant effect of tip diameters between 50 and 100 μm on penetration efficiency. Even at tip diameters lower than 40 μm , i.e. 5–37 μm , no significant difference in penetration efficiencies was observed by Römgers *et al* [36] at the final displacement of the needles. Indeed, this effect can only be valid up to a certain point because, in the same study by Lim *et al* [35], a significant decrease in efficiency was observed when the tip diameter was set at 200 μm . At this point, the penetration efficiency was significantly affected by the tip diameter.

Given the relative effects of the geometrical factors studied on the penetration efficiency, interactions between factors may also be present. As shown in figure S2, there was an observed interaction between D_b and H . The change of D_b from 500 μm to 400 μm did not change the degree of effect of H , but decreasing it further to 300 μm slightly decreases the effect of H on the penetration efficiency, as evident in the change of slope. Moreover, the change in D_b from 300 μm to 500 μm does not affect D_t , but when D_b was set to 400 μm , the degree of effect of D_t on penetration efficiency changed as compared to its effect at $D_b = 300 \mu\text{m}$ and 500 μm . Finally, there was no interaction observed between D_t and H . The presence of interactions between factors led the researchers to analyze a parameter directly dependent on all the geometrical factors mentioned above: the taper angle, α .

Some researchers, such as Kong *et al* [37] and Davis *et al* [19], studied the insertion of MNs into the skin and reported the wall angle (α) as the angle outside the cone. In this study, however, we will refer to α as the internal angle shown in

figure 2(a) and calculated from the different geometrical settings using equation (3). This taper angle depends on all the geometrical factors considered in this study, i.e. base diameter, tip diameter, and radius. If the tip is pointed, when D_t is very close to zero, then α is dependent on H and D_b

$$\alpha = \arctan\left(\frac{D_b - D_t}{H}\right). \quad (3)$$

Plotting the α values of the simulated MN versus their penetration efficiency in figure 3(b) resulted in a general downward trend with increasing angles, although there is a non-linear relationship between them ($R^2 = 0.597$). This indicates that α is not directly proportional to the penetration efficiency and this is due to the different weighted effects of the geometrical factors. This also reinforces the conclusion that basing the design and optimization of MN on the sole α would result in an inaccurate outcome.

Based on these observations, we identified two linear equations for the penetration efficiency as a function of α by adding one more factor and grouping the data by height (figure 4(a)); R^2 values were 0.977 and 0.964 for $H = 600$ and 800 μm , respectively. The plot shows that the penetration efficiency linearly decreases with increasing α . At larger taper angles, the force needed for insertion is higher due to higher resistance, thus decreasing the penetration efficiency [34]. A polynomial model, plotted as a surface plot in figure 4(b), was then fitted to describe the relationship between the taper angle, height, and penetration efficiency (equation (4)):

$$\begin{aligned} \text{Penetration Efficiency} \\ = 1.475\alpha + 0.012H - 0.006H\alpha + 111.9 \end{aligned} \quad (4)$$

Also, the model has a root mean square error (RMSE) of 1.631, thus an acceptable accuracy. Based on the values of the coefficients, α has higher coefficient than H . This implies that

changing the α will have relatively higher impact on the penetration efficiency than a change in height.

Therefore, when designing MNs, H can be set high enough to penetrate the SC without reaching the pain receptors deep in the dermis, and only α needs to be adjusted to optimize the penetration efficiency. With this model that can accurately predict penetration efficiency, the number of geometrical parameters to be considered when designing MN is reduced from three to two.

3. Experimental results

The four prototypes of MN arrays fabricated using two-photon polymerization are shown in the SEM images in figure 5. Since images were taken after the penetration tests to avoid potential effects of the required gold sputter coating on the test results, we can conclude that no deformations occurred on the MN even after penetration on the PDMS skin mimic and that nominal dimensions reported in table 1 were correctly replicated. Aside from the penetration efficiency, the integrity of these microstructures is of paramount importance to ensure that there is no breakage during application that may consequently affect their functionality.

To experimentally validate the numerical simulation results, MN arrays characterized by the four α values were tested for penetration into PDMS. Figure 6 shows the force–displacement plot of all the tested MN arrays. Instead of a plateau at the end of the penetration in the finite element analysis, the end of penetration during the experiment was characterized by a steep increase in slope. Given the experimental setup in which the final displacement had to be set instead of using a constant applied force, data from the experiment are presented as force vs. displacement in figure 6 instead of displacement vs. time, as in figure 3(a). Aside from the penetration efficiency, it is widely known that the insertion force is also a key parameter in estimating the safe use of MNs since a high force can cause the MNs to buckle or break before or during insertion. Nevertheless, after post-processing, the penetration depths of the inserted MNs were acquired, and the penetration efficiencies were calculated.

Similar to the results from the numerical study, albeit in different forms, the plots in figure 6 can also be divided into two zones. The first zone is the penetration of the MNs into the PDMS, characterized by the gradual increase of force with displacement. This continued until a sudden increase in slope which signaled the end of penetration. As seen in the graph, the high increase in force did minimal change in the displacement of the MNs. At this point, the base plate reached the surface of the PDMS further compressing it, thus the small-step continuous increase in displacement. A similar force–displacement profile was obtained by Shu *et al* [32] when they simulated the insertion of an array of solid stainless steel MNs into a substrate with the same properties as the human skin. To validate that Zone 2 was the compression of PDMS, the average slope of the plots in this zone was calculated. This was considered as

the stiffness and was then compared to the expected stiffness of the PDMS used. A relative error of 0.2 was obtained. This error may be due to systematic errors, particularly the usage of different machines and methods in getting the stiffness of both penetration experiments and the characterization of PDMS.

It can also be deduced from figure 6 that MNs with higher tip angles needed more force to be inserted into PDMS. The same observation was presented by the groups of Davis *et al* [19] and Kong *et al* [37] in both experimental and numerical studies. As the angle decreases or as the wall of the MN approaches vertical, a large portion of the total stress becomes oriented along the plane of the MN wall, as compared to stresses normal to the wall, which resulted in an increased insertion force. Like in our numerical study, here we can see that the taper angle has an influence on the insertion force. There was a relatively larger gap in insertion force between MN with angles 25° – 15° compared to angles 15° and 11° . The smaller gap between 15° and 11° may be due to the effect of their height difference, with $\alpha = 11^\circ$ having longer MNs. It was previously mentioned that a longer MN would encounter a greater elastic resistance compared to a shorter MN during penetration, hence needing more force to penetrate the skin. The experiments, while showing that both taper angle and height influence the MN insertion, agree with the numerical study result proving that the taper angle has a stronger influence than the height.

To further validate the numerical study results, the actual and predicted penetration efficiencies of the fabricated MNs with different taper angles are reported in table 2. The penetration efficiency has a maximum for $\alpha = 11^\circ$ and decreases with increasing α . This aligns with the numerical analysis results that also showed the same trend. The predicted penetration efficiencies for each α were also calculated based on the model, and the errors obtained ranged between 3.36% and 16.21%. Moreover, comparing the experimental values to the previously generated model, shown as red triangular dots in supplementary figure S3, a RMSE of 9.3 was obtained. The higher error of the proposed model in predicting the experimental results is due to the approximations the simulation was based on. One factor may be friction. Friction plays an important role in the penetration of the needle into the artificial skin. The higher the friction between the needle and the artificial skin, the higher the resistance and hence the higher penetration force needed to fully insert the needle into the skin. This may lead to incomplete penetration depth and hence, low penetration efficiency. One way to reduce the friction is to coat the MNs, such as with a surfactant. Surfactants can act as wetting agents that help promote the spreading of dermal interstitial fluid along and into the polymer matrix, which leads to boundary lubrication. This consequently reduces the friction of the MN sliding against the skin, thus enabling deeper penetration [38]. Also, in the numerical analysis, only a single needle was considered, while arrays of 4×4 MNs were analyzed in the experiment. As reported in a previous study, the MN density also affects penetration efficiency [15]. Nevertheless, the fit is still acceptable.

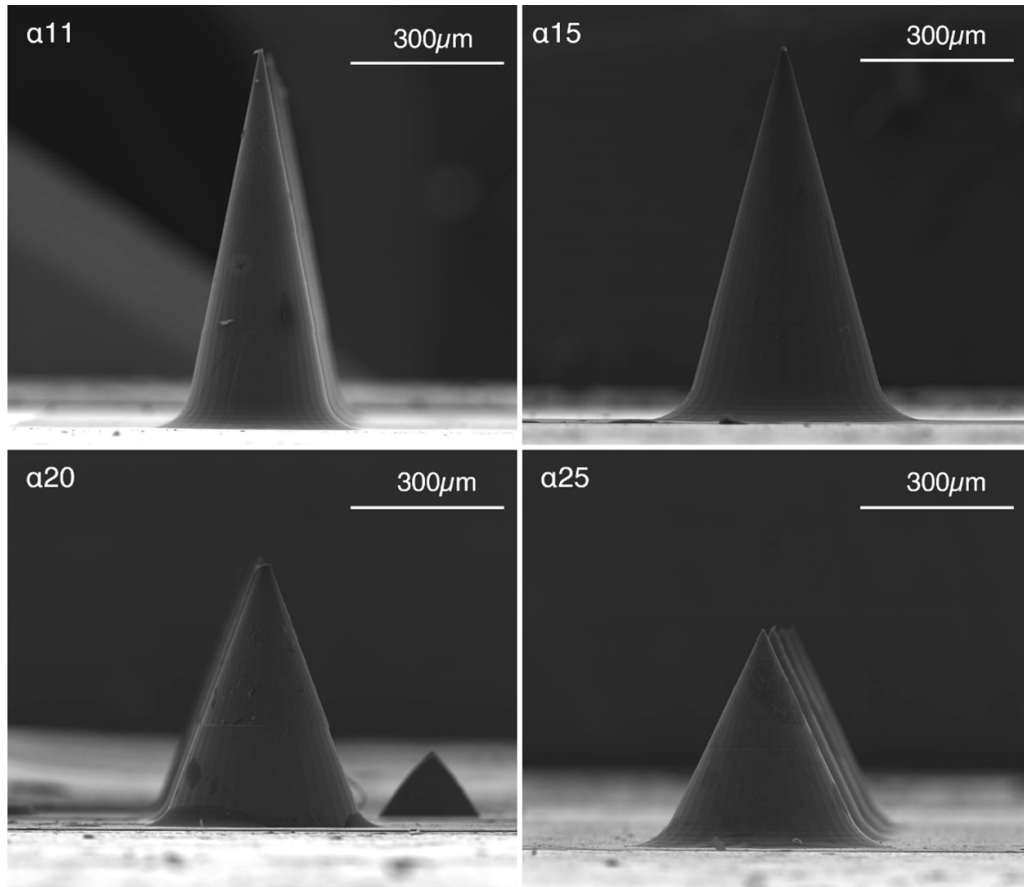


Figure 5. SEM images of the four prototypes of MN arrays after the penetration tests.

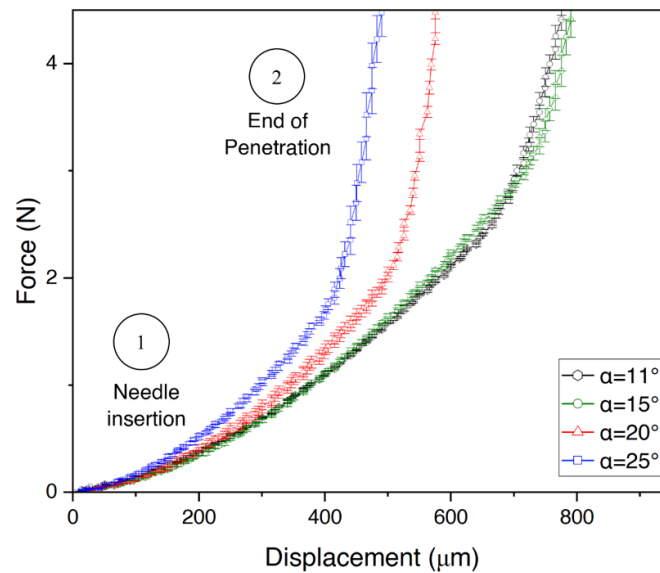


Figure 6. Insertion force as a function of displacement of microneedles with varying α values as they penetrate the PDMS. Zone 1 indicates the penetration of the microneedles into the PDMS, and zone 2 was the end of penetration when only PDMS compression was noted.

Table 2. Actual and predicted penetration efficiencies of the MN with different measured α values.

Measured α , ($^{\circ}$)	Inserted length, (mm)	Designed length, (mm)	Actual penetration efficiency, (%)	Predicted penetration efficiency, (%)	Error, (%)
11.6	0.698	0.771	90.53	84.74	6%
14.7	0.667	0.746	89.41	76.70	14%
20.8	0.463	0.549	84.34	80.74	4%
25.6	0.337	0.429	78.55	88.95	−13%

4. Conclusion

This study has thoroughly analyzed the effects of geometrical factors on the penetration efficiency of solid conical MNs into artificial skin using numerical analysis; these parameters were the base diameter, height, and tip diameter. The penetration of a single solid MN with different geometrical settings into PDMS artificial skin was modeled using finite element analysis. The penetration efficiency was derived from the displacement data of the MN after insertion. The results suggest that the base diameter has the highest influence on penetration efficiency, followed by the height H , and that the tip diameter has no significant effect. The interaction between the factors was also studied, leading to further investigation on the taper angle α , which is dependent on all the previously mentioned geometrical factors. Relating the angle alone with the penetration efficiency did not establish a correlation. However, we proved that by setting a constant height, α has a linear correlation with the penetration efficiency: decreasing α increases the penetration efficiency. A model was first developed based on height and taper angle and on their effects on penetration efficiency, and then experimentally validated. MN arrays with different taper angles were fabricated using two-photon photolithography. Using a tribometer, they were then subjected to a penetration test into a PDMS artificial skin. Both experimental measurements and numerical modeling have shown that two important factors, the taper angle, and height, can be manipulated to predict and optimize the penetration efficiency of solid MN. Furthermore, the results suggest that the taper angle has more influence than the height. To date, no other model has been generated using only these two factors. This can be used to design high penetration efficiency MN arrays for better functionality. H can be set high enough to penetrate the SC without reaching the pain receptors deep in the dermis, and only α needs to be adjusted to optimize the penetration efficiency.

A study is underway to fabricate and replicate the optimized MN arrays using laser ablation and microinjection molding methods to further elucidate the manufacturability limitations of MNs, especially those with very low α values. This study is a stepping stone to realizing highly functional MN arrays and moving forward from numerical analyses and benchtop experiments to large-scale manufacturing.

Data availability statement


All data that support the findings of this study are included within the article (and any supplementary files).

Acknowledgments

The authors thank Monica Voltan for the technical support. Project funded under the BIRD 2020 program sponsored by the University of Padua (Grant No. BIRD201744), and the European Union's Horizon 2020 research and innovation program—Marie Skłodowska-Curie Grant Agreement No. 956097.

ORCID iDs

Kristal Bornillo  <https://orcid.org/0000-0001-8511-9745>

Marco Sorgato  <https://orcid.org/0000-0001-7293-0547>

References

- [1] Ebrahiminejad V, Prewett P D, Davies G J and Faraji Rad Z 2022 Microneedle arrays for drug delivery and diagnostics: toward an optimized design, reliable insertion, and penetration *Adv. Mater. Interfaces* **9** 2101856
- [2] Aldawood F K, Andar A and Desai S 2021 A comprehensive review of microneedles: types, materials, processes, characterizations and applications *Polymers* **13** 2815
- [3] Alkilani A Z, McCrudden M T C and Donnelly R F 2015 Transdermal drug delivery: innovative pharmaceutical developments based on disruption of the barrier properties of the stratum corneum *Pharmaceutics* **7** 438–70
- [4] Holbrook K A and Odland G F 1974 Regional differences in the thickness (cell layers) of the human stratum corneum—an ultrastructural analysis *J. Invest. Dermatol.* **62** 415–22
- [5] Cevc G 2004 Lipid vesicles and other colloids as drug carriers on the skin *Adv. Drug Deliv. Rev.* **56** 675–711
- [6] Williams A C and Barry B W 2012 Penetration enhancers *Adv. Drug Deliv. Rev.* **64** 128–37
- [7] Ita K 2016 Transdermal iontophoretic drug delivery: advances and challenges *J. Drug Target.* **24** 386–91
- [8] Doukas A G and Kollias N 2004 Transdermal drug delivery with a pressure wave *Adv. Drug Deliv. Rev.* **56** 559–79
- [9] Chen Y, Chen B Z, Wang Q L, Jin X and Guo X D 2017 Fabrication of coated polymer microneedles for transdermal drug delivery *J. Control. Release* **265** 14–21
- [10] Henry S, Mcallister D V, Allen M G and Prausnitz M R 1998 Microfabricated microneedles: a novel approach to transdermal drug delivery *J. Pharm. Sci.* (<https://doi.org/10.1021/js980042>)
- [11] Cheung K and Das D B 2016 Microneedles for drug delivery: trends and progress *Drug Deliv.* **23** 2338–54
- [12] Gill H S, Denson D D, Burris B A and Prausnitz M R 2008 Effect of microneedle design on pain in human volunteers *Clin. J. Pain* **24** 585–94
- [13] Sezgin B, Ozel B, Bulam H, Guney K, Tuncer S and Cenetoglu S 2014 The effect of microneedle thickness on pain during minimally invasive facial procedures: a clinical study *Aesthet Surg. J.* **34** 757–65

- [14] Haq M I, Smith E, John D N, Kalavala M, Edwards C, Anstey A, Morrissey A and Birchall J C 2009 Clinical administration of microneedles: skin puncture, pain and sensation *Biomed. Microdevices* **11** 35–47
- [15] Oh J H, Park H, Do K, Han M, Hyun D, Kim C, Kim C, Lee S, Hwang S and Shin S 2008 Influence of the delivery systems using a microneedle array on the permeation of a hydrophilic molecule, calcein *Eur. J. Pharm. Biopharm.* **69** 1040–5
- [16] Bal S M, Kruithof A C, Zwier R, Dietz E, Bouwstra J A, Lademann J and Meinke M C 2010 Influence of microneedle shape on the transport of a fluorescent dye into human skin in vivo *J. Control. Release* **147** 218–24
- [17] Kochhar J S, Quek T C, Soon W J, Choi J, Zou S and Kang L 2013 Effect of microneedle geometry and supporting substrate on microneedle array penetration into skin *J. Pharm. Sci.* **102** 4100–8
- [18] Bal S M, Caussin J, Pavel S and Bouwstra J A 2008 In vivo assessment of safety of microneedle arrays in human skin *Eur. J. Pharm. Sci.* **35** 193–202
- [19] Davis S P, Landis B J, Adams Z H, Allen M G and Prausnitz M R 2004 Insertion of microneedles into skin: measurement and prediction of insertion force and needle fracture force *J. Biomech.* **37** 1155–63
- [20] Li Y, Hu X, Dong Z, Chen Y, Zhao W, Wang Y, Zhang L, Chen M, Wu C and Wang Q 2020 Dissolving microneedle arrays with optimized needle geometry for transcutaneous immunization *Eur. J. Pharm. Sci.* **151** 105361
- [21] De Martino S et al 2022 Effect of microneedles shape on skin penetration and transdermal drug administration *Biomater. Adv.* **142** 213169
- [22] Anbazhagan G, Suseela S B and Sankararajan R 2023 Design, analysis and fabrication of solid polymer microneedle patch using CO₂ laser and polymer molding *Drug Deliv. Transl. Res.* **13** 1813–27
- [23] Uppuluri C T, Devineni J, Han T, Nayak A, Nair K J, Whiteside B R, Das D B and Nalluri B N 2017 Microneedle-assisted transdermal delivery of Zolmitriptan: effect of microneedle geometry, in vitro permeation experiments, scaling analyses and numerical simulations *Drug Dev. Ind. Pharm.* **43** 1292–303
- [24] Martanto W, Moore J S, Couse T and Prausnitz M R 2006 Mechanism of fluid infusion during microneedle insertion and retraction *J. Control. Release* **112** 357–61
- [25] Donnelly R F, Garland M J, Morrow D I J, Migalska K, Singh T R R, Majithiya R and Woolfson A D 2010 Optical coherence tomography is a valuable tool in the study of the effects of microneedle geometry on skin penetration characteristics and in-skin dissolution *J. Control. Release* **147** 333–41
- [26] Marks R 2004 The stratum corneum barrier: the final frontier *J. Nutrition* **134** 2017–21
- [27] Makvandi P et al 2021 Engineering microneedle patches for improved penetration: analysis, skin models and factors affecting needle insertion *Nano-Micro Lett.* **13** 93
- [28] Dąbrowska A K, Rotaru G-M, Derler S, Spano F, Camenzind M, Annaheim S, Stämpfli R, Schmid M and Rossi R M 2016 Materials used to simulate physical properties of human skin *Skin Res. Technol.* **22** 3–14
- [29] Aoyagi S, Izumi H and Fukuda M 2008 Biodegradable polymer needle with various tip angles and consideration on insertion mechanism of mosquito's proboscis *Sens. Actuators A* **143** 20–28
- [30] Yeoh O H 1993 Some forms of the strain energy function for rubber *Rubber Chem. Technol.* **66** 754–71
- [31] Nanoscribe IP-S—NanoGuide *support.nanoscribe.com* (available at: <https://support.nanoscribe.com/hc/en-gb/articles/360001750353-IP-S>)
- [32] Shu W, Heimark H, Bertollo N, Tobin D J, O'Cearbhaill E D and Annaihd A N 2021 Insights into the mechanics of solid conical microneedle array insertion into skin using the finite element method *Acta Biomater.* **135** 403–13
- [33] Verbaan F J, Bal S M, van den Berg D J, Groenink W H H, Verpoorten H, Lüttge R and Bouwstra J A 2007 Assembled microneedle arrays enhance the transport of compounds varying over a large range of molecular weight across human dermatomed skin *J. Control. Release* **117** 238–45
- [34] Ahn B 2020 Optimal microneedle design for drug delivery based on insertion force experiments with variable geometry *Int. J. Control Autom. Syst.* **18** 143–9
- [35] Lim S H, Tiew W J, Zhang J, Ho P C-L, Kachouie N N and Kang L 2020 Geometrical optimisation of a personalised microneedle eye patch for transdermal delivery of anti-wrinkle small peptide *Biofabrication* **12** 035003
- [36] Römogens A M, Bader D L, Bouwstra J A and Oomens C W J 2016 Predicting the optimal geometry of microneedles and their array for dermal vaccination using a computational model *Comput. Methods Biomech. Biomed. Eng.* **19** 1599–609
- [37] Kong X Q, Zhou P and Wu C W 2011 Numerical simulation of microneedles' insertion into skin *Comput. Methods Biomech. Biomed. Eng.* **14** 827–35
- [38] Anjani Q K, Sabri A H B, Utomo E, Domínguez-Robles J and Donnelly R F 2022 Elucidating the impact of surfactants on the performance of dissolving microneedle array patches *Mol. Pharm.* **19** 1191–208